Redox Dynamics of Mixed Metal (Mn, Cr, and Fe) Ultrafine Particles

Peter S. Nico[1*], Benjamin M. Kumfer[2], Ian M. Kennedy[2], Cort Anastasio[3]

[1] Earth Sciences Division, Lawrence Berkeley National Laboratory, One Cyclotron Rd., Berkeley, CA 94720, USA
[2] Department of Mechanical and Aeronautical Engineering, University of California, Davis, CA 95616
[3] Department of Land, Air & Water Resources, University of California, Davis, CA 95616.
[*]Author to whom correspondence should be addressed. Email: psnico@lbl.gov; Tel: 510-486-7118

Abstract

The impact of particle composition on metal oxidation state, and on changes in oxidation state with simulated atmospheric aging, are investigated experimentally in flame-generated nanoparticles containing Mn, Cr, and Fe. The results demonstrate that the initial fraction of Cr(VI) within the particles decreases with increasing total metal concentration in the flame. In contrast, the initial Mn oxidation state was only partly controlled by metal loading, suggesting the importance of other factors. Two reaction pathways, one reductive and one oxidative, were found to be operating simultaneously during simulated atmospheric aging. The oxidative pathway depended upon the presence of simulated sunlight and O_3, whereas the reductive pathway occurred in the presence of simulated sunlight alone. The reductive pathway appears to be rapid but transient, allowing the oxidative pathway to dominate with longer aging times, i.e. greater than ~8 hours. The presence of Mn within the particles enhanced the importance of the oxidative pathway, leading to more net Cr oxidation during aging implying that Mn can mediate oxidation by removal of electrons from other particulate metals.

Introduction

Recent epidemiological studies have demonstrated a correlation between exposure to fine particulate matter and an increased incidence of cardiovascular morbidity and mortality (Samet et al. 2000; Peters et al. 2001; Pope et al. 2004). Unfortunately the mechanisms behind this correlation remain largely unknown. Ultrafine particles (smaller than 100 nm) have been reported to be particularly relevant pathologically due to their small size and high reactivity. The primary constituents of ambient ultrafine particles are carbon, organic compounds and metals (Seinfeld et al. 2003; Herner et al. 2006). The metals, in particular the transition metals, may play a key role in determining the toxicity of ultrafine particles. Of the transition metals, Fe, Cr, and Mn are of particular interest because of their abundance and the fact that their redox chemistry alters their bioavailability and toxicity. Examples of potential sources of Fe, Cr, and Mn in particulate matter include a variety of high energy/combustion sources such as: vehicle exhaust; coal and fuel oil burning; welding fumes and steel processing; and waste incineration (Linak et al. 2000; Antonini et al. 2004; Pascal et al. 2004; Lough et al. 2005; Pekney et al. 2006; Majestic et al. 2007).

In ambient particulate matter from the California Central Valley, Herner et al. (Herner et al. 2006) found Mn and Cr in roughly equal concentrations, ~1.8 ng m^{-3}, with Fe being approximately an order of magnitude more abundant, ~28 ng m^{-3} . Similarly, estimates of emission rates in vehicle exhaust are comparable for Mn and Cr, ~10^{-2} μg km^{-1} $vehicle^{-1}$, with Fe being three orders of magnitude greater (Lough et al. 2005). Single particle analysis of ambient particulate matter from Pittsburgh shows evidence for Fe and Mn within single particles, but the similarity in masses, and the greater abundance of Fe, makes it difficult to quantify these metals based on single particle mass spectrometry. However, based on the chemical similarities

between Mn, Cr, and Fe, and the fact that they are found together in all the sources mentioned above, strongly argues that they are often internally mixed, i.e., found within the same particles.

Iron, Cr, and Mn dynamics within particles are of particular relevance to human health because they are redox active metals whose oxidation states dramatically affect their toxicity. Iron has two major oxidation states under environmentally relevant conditions: Fe(II) and Fe(III). The solubility, and therefore the bioavailability, of Fe(II) is dramatically higher than that of Fe(III); equilibrium concentrations of Fe(III) or Fe(II) from ferrihydrite (am-$Fe(OH)_3$) and am-$Fe(OH)_2$ with pure water are approximately 10^{-5} M and 10^{-10} M, respectively (Cornell et al. 2003, Visual Minteq 2.53). The main mechanism of Fe toxicity is generation of reactive oxygen species (ROS) such as H_2O_2, $^{\bullet}OH$ and $HO_2^{\bullet}$, through Fenton type chemistry (Crichton et al. 2002). Chromium, like Fe, has two major oxidation states, Cr(III) and Cr(VI). Chromium(III) compounds are generally insoluble and non-toxic, whereas Cr(VI), as chromate, is highly soluble, toxic, and potentially carcinogenic (Gad 1989). Manganese has three readily available oxidation states: Mn(II), Mn(III), and Mn(IV). Overall uptake of Mn from pulmonary dosing measured *in vivo* showed absorbed Mn being significantly greater from soluble Mn(II) salts as compared with insoluble Mn(III) and Mn(IV) oxides (Dorman et al. 2001; Aschner et al. 2005). Manganese appears to exert its toxic effects through a variety of pathways including ROS formation, direct oxidation of biological molecules (specifically neurotransmitters) by Mn(III), disruption of cellular Ca, and alterations in Fe homeostasis (Reaney et al. 2005). Therefore, while Mn(II) salts are more bioavailable, the cytotoxicity of Mn(III) compounds appears to be significantly greater than those of Mn(II) (Reaney et al. 2005).

The redox state of these metals within a particle at the time of inhalation will be a function of the source of the particle and changes induced through atmospheric aging. Majestic et al.

(Majestic et al. 2007) used L_{III}-edge X-ray Absorption Spectroscopy (XAS) to show that the Fe in ambient urban aerosol particles was dominated by Fe(III) (> 60%). Forty days of simulated atmospheric aging caused slight increases in Fe(II) for particles larger than 2.5 microns and the opposite trend for 0.25 to 0.50 micron particles. Qi et al. (2003) used K-edge extended X-ray absorption fine structure spectroscopy (EXAFS) to determine that the dominant form of Fe in PM collected in the both urban and rural areas of China was α-Fe_2O_3 (hematite, Fe(III)) with small contributions of Fe(II) in the form of FeO (Qi et al. 2003).

Previous work on pure Cr oxide particles showed that the fraction of Cr(VI) present in laboratory-generated particles is a function of combustion temperature and metal concentration within the flame, with cooler flame temperatures and higher metal concentrations leading to less Cr(VI) (Gao et al. 2002; Werner et al. 2006). Simulated atmospheric aging showed a general tendency for Cr(VI) reduction. Particles generated from a mixed Cr and Fe source showed a decrease in the fraction of Cr(VI) and a change in the dominant form of Cr(III), from a Cr_2O_3/$Cr(OH)_3$ mixture to a mixed Cr-Fe spinel phase (Werner et al. 2006). Subsequent analysis of field particles demonstrated that the Cr-Fe spinel phase was dominant in ambient aerosols, although other phases, including Cr(VI) containing phases, were detected as well (Werner et al. 2007).

Majestic, et al. (Majestic et al. 2007) found that it was difficult to quantify Mn oxidation states in ambient PM due to the tendency of Mn to react rapidly with extraction fluids and/or other redox active components of the PM, e.g. Fe(II). In spite of these difficulties, they determined that oxidized Mn, Mn_{ox} (i.e., Mn(III) and Mn(IV)), accounted for ~30% of the Mn in the fine ($PM_{2.5}$) fraction in ambient aerosol samples from Toronto. Interestingly, Mn_{ox} was absent in the coarse particle fraction, implying that the sources of Mn_{ox} were high

energy/combustion processes. Oxidized Mn was not detected in samples collected from East St. Louis, and the authors state that this could either have been a function of the rapid reduction of Mn upon extraction or a result of a different source profile in this location. Several studies have used K-edge XAS to examine the Mn speciation in aerosol samples generated through combustion of Mn-containing fuel using a gasoline engine with fuel containing MMT (methylcyclopentadienylmanganese tricarbonyl) (Ressler et al. 1999; Ressler et al. 2000; Molders et al. 2001). The major particulate Mn species found in these studies were $MnPO_4$, $MnSO_4$ and Mn_3O_4 (Hausmannite).

The changes in oxidation state caused by atmospheric aging in the studies above are likely due to reactions of particles with reactive photooxidants. The combination of light, water vapor, and ozone in the atmosphere (real or simulated) converts a portion of the O_3 into a cascade of photooxidants dominated by OH, HO_2, and H_2O_2 in the absence of NO_x. These photooxidants can then react with particles (or cloud drops) to cause both oxidation and reduction of metals (Sedlak et al. 1997; Werner et al. 2006).

The goals of the present study are to understand how different combinations of Fe, Cr, and Mn alter the redox states of these metals in freshly generated ultrafine particles and how atmospheric aging affects their redox states. We chose these three metals because they are abundant, have complex redox chemistry, and because changes in their redox states alter their bioavailabilities and toxicities.

Materials and Methods

Particle generation, collection, and aging

A standard laboratory laminar diffusion flame was used as a model nonpremixed combustion system to produce metal oxide nanoparticles. The synthesis method and collection system have been described in more detail in our previous work (Guo et al. 2004; Werner et al. 2006). Briefly, a flame was created by introducing a mixture of 33% hydrogen and 67% argon through a 7.5 mm ID nozzle located along the axis of a vertical wind tunnel containing a constant and uniform flow of air. The total flow rate of the fuel mixture was held constant at 1.6 LPM. A portion of the fuel mixture was diverted through a set of parallel containers wherein vapors of $Fe(CO)_5$, $Cr(CO)_6$ and $Mn_2(CO)_{10}$, were added. The vapor pressures of these metal carbonyls were sufficiently high to achieve the desired concentrations without heating. The precursors were maintained at constant temperature: $Fe(CO)_5$ was kept in an ice bath at 0^oC, while $Cr(CO)_6$ and $Mn_2(CO)_{10}$ were at room temperature. Calibrated mass flow controllers (MKS Instruments, Inc.) were used to control the gas flow through each carbonyl container, allowing for control of the metal oxide aerosol production rate. Samples of the particles were extracted from the flame exhaust using a probe and deposited onto 47 mm PTFE membrane filters (Sartorius AG) using a vacuum. The concentration of Cr in the fuel stream was estimated using vapor pressure data for $Cr(CO)_6$ (Chellappa et al. 2005). The concentrations of Mn and Fe in the fuel stream were derived from the measured particle composition and the fuel stream Cr concentration, with the approximation that all metal introduced into the flame is completely converted to the particle phase.

The atomic metal composition of the particles was measured using a Cameca SX-100 electron microprobe operating at 10 keV with a beam size of 5 μm and a beam current of 20 nA. Samples were prepared for microprobe analysis by transferring a layer of particles from the

PTFE filter to carbon tape. Several areas within each sample were measured and compositional variations due to non-uniformities of the particle layer thickness were found to be insignificant. In addition, a Philips CM-12 transmission electron microscope was used to analyze the particle size and morphology.

Particles collected on filters were aged under simulated atmospheric aging conditions, as previously described (Werner et al. 2006). Samples were aged in a chamber where they were exposed to simulated sunlight (from the filtered output of a 1000 W Xe bulb) and a gas flow of humidified, purified air (~75% RH) either in the presence or absence of 1.6-1.7 ppmv O_3, which was generated from UV illumination of a stream of oxygen. Note that the combination of light, $H_2O(g)$, and O_3 leads to ozone photolysis and subsequent formation of $^{\bullet}OH$, $HO_2^{\bullet}$, and H_2O_2, but that these secondary reactive oxygen species are not be formed in the absence of O_3.

Based on 2-nitrobenzaldehyde actinometry, the photon flux onto the samples was approximately the same as that experienced in the ambient atmosphere in Davis, CA at midday on the summer solstice (i.e., a solar zenith angle of 14°). In contrast, ozone mixing ratios in the chamber were approximately a factor of 10 higher than in polluted atmospheres. Using a simple gas-phase model indicates that concentrations of $^{\bullet}OH$, $HO_2^{\bullet}$, and H_2O_2 in the chamber were approximately 10^8, 10^9, and 10^9 molecules cm^{-3}, respectively, during typical aging conditions. These estimated chamber concentrations of $^{\bullet}OH$ and $HO_2^{\bullet}$ are roughly a factor of 10 higher than typical tropospheric values in midlatitudes during (midday) summer, while the chamber H_2O_2 value is roughly 20 times lower than typical atmospheric levels. Given that some of these species (e.g., $^{\bullet}OH$) can oxidize metals, while others (e.g., $HO_2^{\bullet}$) can reduce metals (Werner et al. 2006), it is difficult to scale our laboratory aging times to aging times in ambient air. Based on the photon and oxidant discussion above, we expect that laboratory aging times roughly

correspond to atmospheric aging times, although this will depend upon which species (light, O_3, $^{\bullet}OH$, $HO_2^{\bullet}$, H_2O_2) is most responsible for a given metal transformation.

The attenuation of light through a particle layer composed of MnO_2 as a function of wavelength was calculated using published values for the optical properties of MnO_2 thin films (Al-Kuhaili 2006). The optical thickness of the particle layer, *t*, was estimated from Eq. 1, where *m* is the weighed particle mass, *A* is the filter deposition area, and ρ is the particle density, which was assigned a value equal to the reported density of bulk MnO_2 (5.0 g/cm^3).

$$t = m / (\rho A) \quad (1)$$

Metal oxidation state and composition analysis by XAS

X-ray absorption data were collected at the Advanced Photo Source (APS) of Argonne National Laboratory. Two different beamlines were employed during different sample runs: Sector 13BM (GSECARS) and Sector 20BM (PNC/XOR). Both beamlines employ Si(111) monochromators and multi-element Ge detectors and were run in unfocused mode, beam size ~1.5 x 6 mm. Both fluorescence and transmission data were collected on all samples and standards; however, the fluorescence data were usually of higher quality for the samples. Energy calibration between samples and between beam runs was maintained by the use of in-line calibration standards placed between the I_1 and I_2 ionization chambers. Natural Mn mineral standards were obtained from the Mineralogical Research Co. and were confirmed using powder XRD (X-ray Diffraction). The data were processed using the data processing programs Athena and Sixpack (Webb 2002; Ravel et al. 2005).

The details of using the height of the Cr XANES (X-ray Absorption Near Edge Structure) pre-edge peak to determine the fraction of Cr(VI) within the particles is described elsewhere (Werner et al. 2006). Since we used similar methods here, we assume the same absolute precision for our measurements, approximately ± 1%. The average Mn oxidation state in the samples was determined using a standard curve prepared in a manner analogous to (Ressler et al. 1999), i.e. by fitting an arctangent function to the normalized spectra and plotting the center point of the function versus the oxidation state of known compounds. Because structural changes can induce small shifts in edge position independent of average oxidation state, it was important to include standards that had the same formal oxidation state but different structures (we used two Mn(II) and three Mn(III) standards), as well as the same standard run at different locations (two Mn(IV) spectra). Using these seven standards an excellent correlation was obtained, $R^2 = 0.9977$, with a slope and intercept of 0.30 eV^{-1} and 1900 eV, respectively. The standard deviation about the calculated line is ~0.15 eV, which indicates that changes in edge position larger than 0.15 eV are most likely due to changes in oxidation state. Calculated in terms of Mn oxidation state, this corresponds to a change in oxidation state of 0.04 units. The error bars represent the standard deviation associated with the determination of Mn oxidation state are set at this 0.04 value.

Principal component analysis applied to 59 Mn sample XANES spectra showed that the variation within the samples could be well reproduced with only 6 components. The IND function reached a minimum at 7 components, but visual inspection of the sample spectra in comparison to the reconstructed spectra showed that all the sample spectra were very well reproduced using only 6 components. Using these 6 components, target transformations were performed using all the standard Mn spectra collected. Of the 12 spectra tested, four met the

SPOIL < 3 criteria outlined by Beauchemin, et al (2002): Pyrochroite ($Mn(OH)_2$), Hausmannite (Mn_2O_3), Ramsdellite (γ-MnO_2), and $MnSO_4$. Unfortunately, of these spectra all but $MnSO_4$ are compromised by an imperfect match of their XRD patterns to standard values. The pyrochroite spectra showed strong contributions of both pyrochroite peaks and hausmannite peaks, whereas the XANES and EXAFS spectra of the hausmannite and pyrochroite standards were nearly identical. The XRD pattern of the hausmmanite standard also appeared to show a minor contribution of pyrochroite along with the peaks expected for hausmannite. The ramsdellite XRD pattern showed many of the major ramsdellite peaks, but also a number of other peaks. In spite of the imperfect standards, linear combination fits were attempted using the hausmannite, ramsdellite, and $MnSO_4$ standards. Hausmannite was chosen over pyrochroite because its XRD pattern was the least convoluted, and the use of both the pyrochroite and hausmannite standard made any interpretation of the fitting results impossible. The fraction attributed to $MnSO_4$ in the fits is reported below simply as Mn(II) fraction because the XANES spectra of Mn(II) salts are not very distinct from each other.

Linear combination fitting of Fe EXAFS were undertaken using five Fe standards, γ-Fe_2O_3 (maghemite), Fe_3O_4 (magnetite), α-Fe_2O_3 (hematite), $FeCr_2O_4$ (chromite) and $Fe(OH)_3$ (ferrihydrite). Except for $Fe(OH)_3$ and α-Fe_2O_3, the remaining standards all have the same crystal structure and differ only by the presence or absence of Fe(II) and/or Cr(III) centers. The $Fe(OH)_3$ is a short range order Fe(III) (hydr)oxide that is a good representation for disordered Fe (hydr)oxide materials present either as discrete phases or as disordered regions within otherwise crystalline Fe (hydr)oxides. The k^3 weighted Fe chi functions were fit over a range from 2.6 to 10. The percentages obtained from the fittings were used to calculate average Fe oxidation state based on the ideal formulas of the above standards.

Results

Composition effect on initial conditions

TEM (transmission electron microscopy) images of flame-generated mixed metal oxide particles are shown in Figures 1a and b. The particles shown in Figure 1a consist of a mixture of Cr and Mn oxides generated from a fuel stream containing a total metal concentration of approximately 25 ppmv. Typical of flame-generated materials, the particles are aggregates of smaller primary particles, here with diameters < 10 nm. As shown in Figure 1b, the addition of Fe to this mix results in primary particles that appear to cluster roughly into two size ranges. In this case, the total metal concentration is larger by an order of magnitude, roughly 260 ppmv, indicating that the particle size distribution is dependent upon initial precursor concentration. The bimodal characteristic is consistent with previous observations of chromium oxide (Guo et al. 2004) and iron oxide (Guo et al. 2007) particles produced using this method. In a past study of Cr oxide particle formation, a bimodal distribution was found to result only when the precursor concentration was sufficiently high (Guo et al. 2004). The bimodal distribution is believed to occur as a result of two separate particle nucleation events: the larger mode corresponding to nucleation occurring on the fuel side of the location of maximum temperature, and the smaller mode arising on the oxygen side.

Another effect of precursor concentration is that the fraction of Cr(VI) within the particles decreases with increasing total metal concentration, as shown in Figure 2a. This result is true whether the fuel contained one metal (Cr only), two metals (Cr and Mn), or three metals (Cr, Mn and Fe) and appears to be largely independent of the relative ratios of the metals. This is consistent with the Cr-only results of Guo and Kennedy (2004), where the initial fraction of

Cr(VI) within the particles was determined largely by the total metal concentration (Guo et al. 2004). In that work, it was found that increasing the Cr precursor concentration leads to increased formation of Cr(III) oxide particles on the fuel-side of the flame, which ultimately results in a lower fraction of Cr(VI) in the product aerosol. While this relationship appears generally true, the importance of total metal concentration becomes less important after a threshold of ~100 ppmm total metal. As seen in Figure 2b, the relationship between Mn oxidation state and metal precursor concentration is more complex than that for Cr, implying that there are additional factors controlling the Mn oxidation state, e.g., the ratios of the metal precursors in the fuel, phase transitions, etc. Unfortunately, due to experimental constraints, the absolute concentration of Mn in the fuel mixture must remain constant for all samples while the concentration of Cr is varied to alter the Cr to Mn ratio. For this reason, the relationship shown in Figure 2b for the Cr and Mn particles could also be interpreted as a function of percent Mn in the flame.

Simulated atmospheric aging of mixed Cr and Mn particles

The impact of atmospheric aging on particle reactivity and metal oxidation state may be as important as the conditions under which the particles were formed. Although the total magnitude of the observed changes in redox state are generally small, these changes are almost certainly concentrated at the surface of the particles, and since it is the surface of the particles that will control their reactivity in a biological system, small measured changes may represent significant changes in particle toxicity or metal bioavailability. As seen in Figures 3a and b, simulated atmospheric aging with the inclusion of O_3 induces changes in both the Cr and Mn oxidation states, in this case for particles with a Mn to Cr atomic ratio of 36:64. This ratio of Mn and Cr amounts is consistent with the results of Herner at al. (2006) who reported average Mn

and Cr concentrations of the same order of magnitude. As shown in Figures 3a and b, the effect of aging on the magnitude and direction of the oxidation state changes is influenced by the amount of particles collected on the filters. Although the true line shapes associated with the data in Figure 3a and b are unknown, straight lines have been fit to the data and a linear rate extracted, Figure 3c, in order to aid discussion and make trends more apparent. The filters with the lowest particle load (~ 0.3 mg) show oxidation of both Cr and Mn during aging, whereas the filters with the heaviest load (~ 1 mg) show a net reduction of Cr and almost no change in Mn oxidation state. Results for the 0.6 mg loading sample are intermediate between those for the 0.3 mg and the 1.0 mg samples. The overall changes in Mn oxidation state are small compared with the error bars, but the changes in Cr(VI) percentage are more significant. Importantly, in the 0.3 mg system both elements show net oxidation indicating that the oxidation state changes are being induced by an external reactant acting as a net sink for electrons from the Cr and Mn in the particles. In contrast, the movement of electrons between the two metals would result in the oxidation of one metal but the reduction of the other. However, this does not preclude one element acting as a redox mediator, e.g., oxidation of one metal, which subsequently reacts with the other metal.

The change in linear rate for both Cr and Mn oxidation can be seen in Figure 3c. There is an approximately linear relationship between the linear rates and the filter loading, with lighter loadings showing more oxidation and heavier loadings showing reduction. The figure shows that at any given loading Mn is more likely to show net oxidation (positive rate) as compare to Cr, implying that Mn is more easily oxidized. The sensitivity of change in the oxidation state to particle loading suggests that there are two competing reaction pathways activated by the simulated atmospheric aging: one pathway that drives both elements toward oxidation but is

attenuated as the particles become more thickly packed; and a second that drives both elements toward reduction and is enhanced as the particles become more thickly loaded. Although this particle loading effect is an artifact of our experimental technique, it has serendipitously provided a clear illustration of the two competing effects. The nature of these effects is not entirely clear, but will be discussed in more detail later. For the moment, it is sufficient to point out that if one extrapolates to an "isolated" or free particle, i.e. particle loading approaching zero, atmospheric aging would tend to cause the oxidation of both Cr and Mn in these binary metal particles.

Simulated Atmospheric Aging of Particles with Varying Compositions

The presence of two competing reaction pathways (oxidative and reductive) can be seen as a function of time in Figure 4, which shows the changes in oxidation state for a mixed Cr and Mn particle with a Mn/Cr ratio of 1.6 (diamonds), and in a ternary Mn, Cr, Fe particle with an atomic metal composition of 1% Cr, 3% Mn and 96% Fe (squares). The ternary particle was designed to better reproduce ambient aerosol particles in which Fe is found with an abundance that is one to two orders of magnitude greater than Cr or Mn. As shown in Figure 4a, in both samples there is a period of initial reduction of Cr followed by oxidation. The changes in Mn (Figure 4b) are less dramatic, but they too show slight initial reduction followed by oxidation at longer times, i.e. >8 hrs. As is true for the results shown in Figure 3, the aging-induced changes in Cr and Mn oxidation states shown in Figure 4 are highly correlated ($R = 0.98$ and 0.96 for the 38% Cr and 1% Cr samples, respectively), showing that the overall changes in Cr and Mn oxidation state are being driven by an external reactant. These aging results imply that the reduction pathway is either transient or has a shorter induction period when compared with the oxidative pathway.

Linear combination fitting of the EXAFS iron signal from Figure 4 confirms that, as previously reported, the dominant Fe crystal structure was the γ-Fe_2O_3/Fe_3O_4 spinel structure (Guo et al. 2007). However, the fits did indicate a small fraction of disordered material (0-20%) and the presence of reduced centers within the γ-Fe_2O_3/Fe_3O_4 spinel structure that are indicated by an average Fe oxidation state of between 2.9 and 3.0. This Fe speciation was similar for all samples.

The effect of varying the relative amounts of Cr and Mn on changes in oxidation state during aging is shown in Figure 5. While there is significant scatter in the data, there appears to be a trend towards greater net oxidation of both Cr and Mn with increasing Mn content, implying an important role for Mn in capturing oxidative potential from atmospheric reactants and passing it to other elements within a particle. This result becomes more pronounced if one accounts for the rapid initial reduction of Cr seen in the 63% Mn particles in Figure 4a, a result that was not observed in particles containing less Mn. Specifically, the open square on Figure 5 represents the change in Cr oxidation state for these particles between time points 16 hrs and 24 hrs. Similarly, because the thermodynamic driving force for oxidation should diminish as the net oxidation state of the particle increases and the kinetic driving force for reduction should increase as the concentration of oxidized Mn centers increases, the smaller degree of oxidation of the 100% Mn particle could be a result of the significantly higher initial average oxidation state for this system as compared to the mixed metal particles. The data in Figure 5 again show that both Cr and Mn can be oxidized at the same time confirming the involvement of an external oxidant. In addition, the fact that the presence of more Mn tends to drive Cr toward oxidation implies a mechanism by which Mn is oxidized and then reacts with Cr(III) causing the oxidation of the Cr(III) to Cr(VI).

Aging without ozone

The results of aging particles with simulated sunlight in humidified air without ozone provide further insight into the identities of the two different reaction pathways. The results (Figure 6a and b) show that in the absence of O_3, both Cr and Mn are reduced after 24 hours of illumination, generally independent of particle composition. For Mn (Figure 6b), the extent of reduction was similar across particles of all compositions. However, for Cr, the reduction is similar for the Cr and Mn particles, but much more extensive for the Cr/Mn/Fe particles. For comparison, the results of aging the same particles with and without ozone are also shown. The addition of ozone leads to a net oxidation of both Mn and Cr, except in the 72% Cr, 28% Mn case, where there is a net reduction of Cr, although less reduction than in the absence of O_3.

Mn structural Identification

Principal component analysis indicated that six distinct phases could account for the variation within the particles. Linear combinations using the three phases identified by target transformation (Mn(II) phase(s) ($MnSO_4$), mixed Mn(II)/Mn(III) phase(s) (hausmannite), and Mn(IV) phase(s) (ramsdellite)) yielded good reproductions of the edge shape for the 100% Mn particles as well as the two other samples with the greatest Mn to Cr ratios (63% Mn-38%Cr and 56%Cr-44% Mn). The form of Mn in these samples is dominated by a mixed Mn(II)/Mn(III) phase and a Mn(IV) phase, with a small contribution of Mn(II) phases (Table 1). Interestingly, the changes upon aging appear to involve mostly interconversion of Mn(III) and Mn(IV) as opposed to increases or decreases in the Mn(II) fraction. The unsatisfactory linear combination fits for particles with greater percentages of Fe and Cr suggests that the additional components indicated by the PCA, but not identified by target transformation, probably include mixed Mn, Cr, and/or Fe phases.

Discussion

In our previous work that studied the redox chemistry of Cr, we invoked a simple conceptual model of a particle in which a solid core is surrounded by a liquid-like layer, and suggested that the chemical changes in the particle take place either in this liquid layer or at the boundary between the water and the solid surface. In this previous study, pure Cr particles and mixed Cr/Fe particles showed a tendency toward reduction during atmospheric aging. These results were explained by a combination of the low solubility and kinetic stability of Cr(III) compounds and the ability of HO_2 to reduce Cr(VI) to Cr(III), resulting in the net reduction of Cr(VI) to Cr(III). The fact that in the current study we observe significant oxidation of Cr implies that either the filter loadings were significantly different between the two studies or that the presence of Mn in these particles has significantly altered their net reactivity.

Therefore, in order to expand our conceptual model, we must first focus on the redox chemistry of Mn. As stated above, the results indicated that there are at least two reactive pathways operating on the particles during simulated atmospheric aging: an oxidative pathway in the presence of light and ozone, and a reductive pathway caused by light in the absence of ozone (Figures 3 and 6). The oxidative pathway is clearly linked to the presence of O_3, since oxidation of Mn (and Cr) is only seen when O_3 is included. The combination of light and ozone produces a trio of gas-phase oxidants that can partition into the particle liquid layer and react with the metals. Based on estimated concentrations of gas-phase oxidants in the aging chamber, and their Henry's law constants, we estimate that the concentrations of reactants in the liquid-like aqueous layers are approximately: $^{\bullet}OH$ (10^{-10} M), $HO_2^{\bullet}$ (10^{-7} M), and H_2O_2 (10^{-5} M). Both $^{\bullet}OH$ and $HO_2^{\bullet}$ are thermodynamically capable of oxidizing hausmannite to MnO_2, with a ΔG^0 of approximately

-700 and -200 kJ/mol, respectively. While H_2O_2 has an extremely complex chemistry with Mn, it is also thermodynamically capable of oxidizing hausmannite to MnO_2, with a ΔG^0 of approximately -320 kJ/mol. (For the above calculations, ΔG^0 for β-MnO_2 was used in place of that for ramsdellite (γ-MnO_2). This is a good assumption given the similarity in structure and the tendency of β-MnO_2 and γ-MnO_2 to be intermixed. (Parker et al. 2003; Ruebush et al. 2006)). Importantly, in contrast to Cr, the reduced species of Mn (i.e., Mn(II)) is more soluble than its oxidized state, making it more available for oxidation both at the solid surface and in the surrounding liquid layer, while the oxidized species (Mn(III) and Mn(IV)) are less soluble, making them potentially less available for reduction.

The reductive pathway is more important at shorter time points and is enhanced relative to the oxidative pathway as the particles become more thickly packed (i.e., with greater filter loadings). The reductive pathway could involve either trace concentrations of reductants such as volatile organic compounds (VOCs) within the chamber, or, more likely, transfer of an electron from water to the metal because of illumination. It is well known that the water oxidizing center of photosystem II is an oxo-bridge Mn cluster; simpler Mn compounds – both solids and clusters in solution – have also shown the ability to oxidize water upon illumination (Dzhabiev et al. 1976; Elizarova et al. 2000; Yano et al. 2006). Iron (hydr)oxides have also shown this ability (Faust et al. 1990); it is probable that Cr compounds, being isoelectronic with Mn(IV), would also have a similar ability (Elizarova et al. 2000). In addition, it has been shown that Cr(VI) may participate in the photo-oxidation of water mediated by TiO_2 (Kajitvichyanukul et al. 2005).

The competition between the oxidative and reductive pathways is both a function of filter loading (Figure 3) and time (Figure 4). The dependence on particle layer thickness could potentially be explained by the oxidation and reduction pathways having different wavelength

dependencies. Figure 7 shows the attenuation of light through a Mn oxide film for different filter loadings. For higher loadings (i.e., thicker particle layers), near-UV light is significantly attenuated. Therefore, increased loading could cause diminished light-driven production of oxidizing ROS species in deeper layers because O_3 photolysis is limited to wavelengths of light below 330 nm. In contrast, the theoretical wavelength limit for water conversion to O_2 and H_2 is $\leq$1008 nm. For example, 405 nm light has been used to induce the oxidation of water by Mn(IV) species in acidic solution (Dzhabiev et al. 1976; Elizarova et al. 2000). These longer wavelengths are significantly less attenuated than light at 330 nm (Figure 7). The observation that the oxidative pathway becomes dominant at longer times (Figure 4) could be explained in several ways. For example, the oxidation of water could become less favorable as metals at the surface of the particles are reduced. Whatever detailed mechanisms are involved, it is important to note for environmental significance that individual or small groups of particles in natural systems represent the extreme low loading case and are therefore much more susceptible to oxidation than under the conditions presented here.

As mentioned above, previous research showed no tendency for oxidation of Cr in either pure Cr or mixed Cr-Fe particles during atmospheric aging (Werner et al. 2006), while the current study shows frequent examples of net Cr oxidation in the presence of Mn. In addition, Figure 3c shows that at any given particle loading, Mn is more likely to show net oxidation when compared to Cr. These observations, combined with the fact that the extent of Cr oxidation after 24 hr tends to increase as a function of Mn content in the particles (Figure 5), indicate that the presence of Mn drives the oxidation of Cr, i.e. that Mn is acting as a source of oxidative potential for the particle. This result is significant to the extent that it shows that, independent of any net

changes in Mn oxidation state, the presence of Mn in mixed composition particles could have a significant effect on the oxidation state of the other species in the particle.

Conclusions

The chemistry and interactions between Cr, Mn, and Fe are of particular interest because changes in oxidation state will result in changes in the bio-availabilities and toxicities of these metals. The apparent ability of Mn to capture oxidative potential and pass it on to other fractions of the particle, e.g., Cr, Fe, or possibly organics, shows that the presence of Mn in particles will generally make those particles more oxidized and oxidizing. In the case of Cr, Mn will cause a significant increase in the toxicity of the particles because it will lead to a higher percentage of Cr(VI); the fact that this Cr(VI) is likely on the particle surface, and is easily soluble, exacerbates the potential for particle toxicity. For Fe, a more oxidized particle generally means lower amounts of soluble Fe. Manganese in the mixed metal particles is present in all three of its possible oxidation states (Mn(II), Mn(III), and Mn(IV)), leading to the conclusion that inhaled Mn particles will present to the lungs both a readily bio-available, soluble Mn(II) fraction as well as a highly oxidizing Mn(III)/Mn(VI) fraction. The impact of aging on Mn speciation indicated that the particles are likely to become more oxidizing with residence time in the atmosphere, making them initially more reactive when inhaled. The impact of Mn on the toxicity of other particulate matter components will depend on whether those components become more or less toxic with oxidation.

Acknowledgments

This publication was made possible by grant number 5 P42 ES004699 from the National Institute of Environmental Health Sciences (NIEHS), NIH and the contents are solely the responsibility of the authors and do not necessarily represent the official views of the NIEHS, NIH. Additional support was provided by the California Agricultural Experiment Station (Project CA-D*-LAW-6403-RR). PNC/XOR facilities at the Advanced Photon Source, and research at these facilities, are supported by the US Department of Energy - Basic Energy Sciences, a major facilities access grant from NSERC, the University of Washington, Simon Fraser University and the Advanced Photon Source. GeoSoilEnviroCARS is supported by the National Science Foundation-Earth Science (EAR-0622171), Department of Energy-Geosciences (DE-FG02-94ER14466) and the State of Illinois. Use of the Advanced Photon Source is also supported by the U. S. Department of Energy, Office of Science, Office of Basic Energy Sciences, under Contract DE-AC02-06CH11357. Partial support was provided by U.S. Department of Energy, Office of Biological and Environmental Research, Environmental Remediation Sciences Program under contract no. DE-AC02-05CH11231. The authors thank the Electron Microprobe Lab at UCD (http://microprobe.geology.ucdavis.edu/) for assistance in conducting the composition analysis.

References

Al-Kuhaili, M. F. (2006). Chemical and optical properties of thermally evaporated manganese oxide thin films. *Journal of Vacuum Science & Technology A* 24: 1746-1750.

Al-Kuhaili, M. F. and S. M. A. Durrani (2007). Optical properties of chromium oxide thin films deposited by electron-beam evaporation. *Optical Materials* 29: 709-713.

Antonini, J. M., M. D. Taylor, et al. (2004). Pulmonary Responses to Welding Fumes: Role of Metal Constituents. *Journal of Toxicology and Environmental Health, Part A* 67: 233 - 249.

Aschner, M., K. M. Erikson, et al. (2005). Manganese dosimetry: Species differences and implications for neurotoxicity. *Critical Reviews in Toxicology* 35: 1-32.

Chellappa, R. and D. Chandra (2005). Assessment of vapor pressure data of solid metal carbonyls. *The Journal of Chemical Thermodynamics* 37: 377-387.

Cornell, R. M. and U. Schwertmann (2003). The Iron Oxides: Structure, Properties, Reactions, Occurrences and Uses, Wiley-VCH.

Crichton, R. R., S. Wilmet, et al. (2002). Molecular and cellular mechanisms of iron homeostasis and toxicity in mammalian cells. *Journal of Inorganic Biochemistry* 91: 9-18.

Dorman, D. C., M. F. Struve, et al. (2001). Influence of particle solubility on the delivery of inhaled manganese to the rat brain: Manganese sulfate and manganese tetroxide pharmacokinetics following repeated (14-day) exposure. *Toxicology and Applied Pharmacology* 170: 79-87.

Dzhabiev, T. S. and V. Y. Shafirovich (1976). Photooxidation of Water by Manganese(Ii) Sulfate. *Reaction Kinetics and Catalysis Letters* 4: 419-423.

Elizarova, G. L., G. M. Zhidomirov, et al. (2000). Hydroxides of transition metals as artificial catalysts for oxidation of water to dioxygen. *Catalysis Today* 58: 71-88.

Faust, B. C. and J. Hoigne (1990). Photolysis of Fe(III)-hydroxyl complexes as sources of OH radicals in clouds, fog, and rain. *Atmospheric Environment* 24A: 79-89.

Gad, S. C. (1989). Acute and Chronic Systemic Chromium Toxicity. *Science of the Total Environment* 86: 149-157.

Gao, Y., E. D. Nelson, et al. (2002). Characterization of atmospheric trace elements on PM2.5 particulate matter over the New York-New Jersey harbor estuary. *Atmospheric Environment* 36: 1077-1086.

Guo, B. and I. M. Kennedy (2004). The speciation and morphology of chromium oxide nanoparticles in a diffusion flame. *Aerosol Science and Technology* 38: 424-436.

Guo, B. and I. M. Kennedy (2007). Gas-phase flame synthesis and characterization of iron oxide nanoparticles for use in a health effects study. *Aerosol Science and Technology* 41: 944-951.

Herner, J. D., P. G. Green, et al. (2006). Measuring the trace elemental composition of size-resolved airborne particles. *Environmental Science & Technology* 40: 1925-1933.

Kajitvichyanukul, P. and C. Changul (2005). Photocatalytic removal of tri- and hexa-valent chromium ions from chrome-electroplating wastewater. *ASEAN Journal Science and Technology Development* 22: 355-363.

Linak, W. P., C. A. Miller, et al. (2000). Comparison of particle size distributions and elemental partitioning from the combustion of pulverized coal and residual fuel oil. *Journal of the Air & Waste Management Association* 50: 1532-1544.

Lough, G. C., J. J. Schauer, et al. (2005). Emissions of Metals Associated with Motor Vehicle Roadways. *Environ. Sci. Technol.* 39: 826-836.

Majestic, B. J., J. J. Schauer, et al. (2007). Application of synchrotron radiation for measurement of iron red-ox speciation in atmospherically processed aerosols. *Atmospheric Chemistry and Physics* 7: 2475-2487.

Majestic, B. J., J. J. Schauer, et al. (2007). Development of a manganese speciation method for atmospheric aerosols in biologically and environmentally relevant fluids. *Aerosol Science and Technology* 41: 925-933.

Molders, N., P. J. Schilling, et al. (2001). X-ray fluorescence mapping and micro-XANES spectroscopic characterization of exhaust particulates emitted from auto engines burning MMT-Added gasoline. *Environmental Science & Technology* 35: 3122-3129.

Parker, S. C., S. Kerisit, et al. (2003). Modelling inorganic solids and their interfaces: A combined approach of atomistic and electronic structure simulation techniques. *Faraday Discussions* 124: 155-170.

Pascal, L. E. and D. M. Tessier (2004). Cytotoxicity of chromium and manganese to lung epithelial cells in vitro. *Toxicology Letters* 147: 143-151.

Pekney, N. J., C. I. Davidson, et al. (2006). Identification of sources of atmospheric PM at the Pittsburgh Supersite, Part 1: Single particle analysis and filter-based positive matrix factorization. *Atmospheric Environment* 40: S411-S423.

Peters, A., D. W. Dockery, et al. (2001). Increased particulate air pollution and the triggering of myocardial infarction. *Circulation* 103: 2810-5.

Pope, C. A., M. L. Hansen, et al. (2004). Ambient particulate air pollution, heart rate variability, and blood markers of inflammation in a panel of elderly subjects. *Environmental Health Perspectives* 112: 339-345.

Qi, J. H., M. P. Zhang, et al. (2003). An EXAFS study on the local structure around iron in atmospheric aerosols collected in the Qingdao area. *Molecules* 8: 31-39.

Ravel, B. and M. Newville (2005). ATHENA, ARTEMIS, HEPHAESTUS: data analysis for X-ray absorption spectroscopy using IFEFFIT. *Journal of Synchrotron Radiation* 12: 537-541.

Reaney, S. H. and D. R. Smith (2005). Manganese oxidation state mediates toxicity in PC12 cells. *Toxicology and Applied Pharmacology* 205: 271-281.

Ressler, T., J. Wong, et al. (1999). Manganese speciation in exhaust particulates of automobiles using MMT-containing gasoline. *Journal of Synchrotron Radiation* 6: 656-658.

Ressler, T., J. Wong, et al. (2000). Quantitative speciation of Mn-bearing particulates emitted from autos burning (methylcyclopentadienyl)manganese tricarbonyl-added gasolines using XANES spectroscopy. *Environmental Science and Technology* 34: 950-958.

Ruebush, S. S., G. A. Icopini, et al. (2006). In vitro enzymatic reduction kinetics of mineral oxides by membrane fractions from Shewanella oneidensis MR-1. *Geochimica et Cosmochimica Acta* 70: 56-70.

Samet, J. M., F. Dominici, et al. (2000). Fine particulate air pollution and mortality in 20 U.S. cities, 1987-1994. *N Engl J Med* 343: 1742-9.

Sedlak, D. L., J. Hoigné, et al. (1997). The cloudwater chemistry of iron and copper at Great Dun Fell, UK. *Atmospheric Environment* 31: 2515-2526.

Seinfeld, J. H. and J. F. Pankow (2003). Organic Atmospheric Particulate Material. *Annual Review of Physical Chemistry* 54: 121-140.

Webb, S. (2002). SixPack. Stanford, Sam Webb.

Werner, M., P. Nico, et al. (2006). Laboratory study of simulated atmospheric transformations of chromium in ultrafine combustion aerosol particles. *Aerosol Science and Technology* 40: 545-556.

Werner, M. L., P. S. Nico, et al. (2007). Use of Micro-XANES to speciate chromium in airborne fine particles in the Sacramento valley. *Environmental Science and Technology* 41: 4919-4924.

Yano, J., J. Kern, et al. (2006). Where water is oxidized to dioxygen: Structure of the photosynthetic Mn4Ca cluster. *Science* 314: 821-825.

List of Figure and Table Captions

Figure 1 TEM images of flame-generated mixed metal oxide nanoparticles (a) 64% Cr, 36% Mn (mole ratio) (b) 91% Fe, 6% Cr, 3% Mn (mole ratio).

Figure 2 Changes in initial Cr and Mn oxidation state as a function of total metal concentration in the flame. Absolute Mn concentration in the fuel is the same for all samples, while Cr and Fe concentrations are varied to produced different compositions and total metals concentrations.

Figure 3 Effect of particle aging on the oxidation states of Cr (A) and Mn (B) as a function of filter loading, (C) change in Cr and Mn linear oxidation rate during aging as a function of filter loading. Positive values represent oxidation, while negative values represent reduction. Particle composition is 64% Cr and 36% Mn. The 16 hr point for the 0.3 mg sample was excluded when calculating the slopes reported in C. However, even when it is included, the correlation coefficients for the slopes as a function of filter loading (C) are still high at 0.885 and 0.999 for Mn and Cr, respectively.

Figure 4 Changes in Cr and Mn oxidation state as a function of time showing initial reduction followed by oxidation. Milligrams of particles per filter are shown along with Cr and Mn mole percentages.

Figure 5 Change in Cr(VI) fraction and Mn oxidation state after 24hrs of full atmospheric aging as a function of Mn content. Open square indicates the change in Cr oxidation state between 16 hrs and 24 hrs for the 63% Mn particles. Positive values represent oxidation while negative values correspond to reduction. Filter loadings range from 0.5-0.7 mg/filter.

Figure 6 Comparison between aging without ozone and aging with ozone. Particle loadings are between 0.6-0.7 mg/filter.

Figure 7 Fraction of transmitted light through a layer of Mn oxide particles as a function of wavelength and filter loading.

Table 1 Linear combination fitting results of Mn only and mixed Mn/Cr particles. Times refer to the duration of simulated atmospheric aging (light, H_2O(g), and ozone).

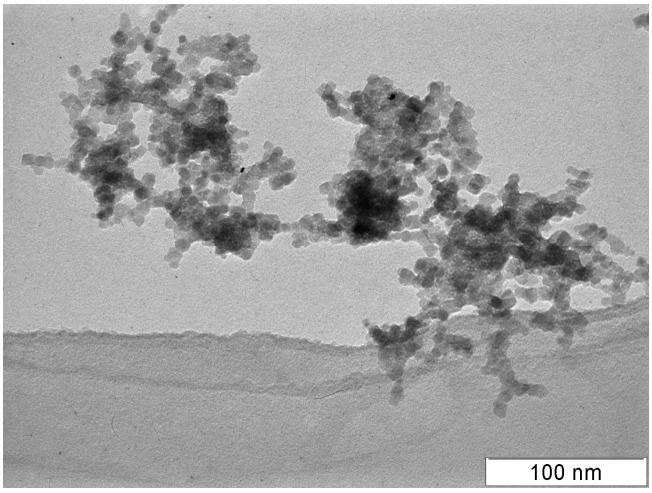

(a)

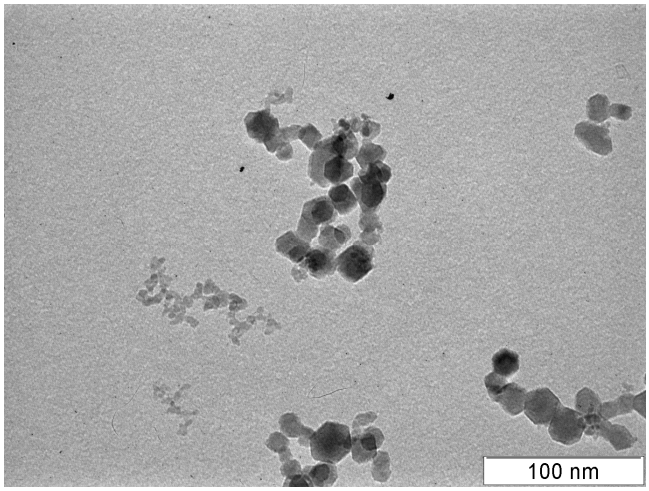

(b)

Figure 1

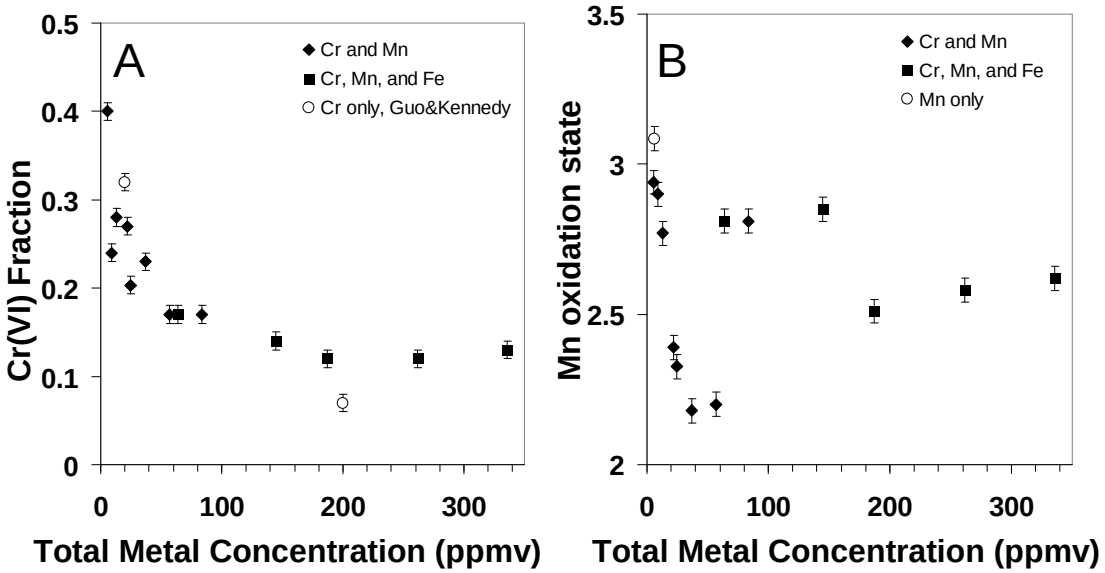
A
Cr and Mn
Cr, Mn, and Fe
Cr only, Guo&Kennedy
Cr(VI) Fraction
0.5
0.4
0.3
0.2
0.1
0
0
100
200
300
Total Metal Concentration (ppmv)
B
Cr and Mn
Cr, Mn, and Fe
Mn only
Mn oxidation state
3.5
3
2.5
2
0
100
200
300
Total Metal Concentration (ppmv)

Figure 2

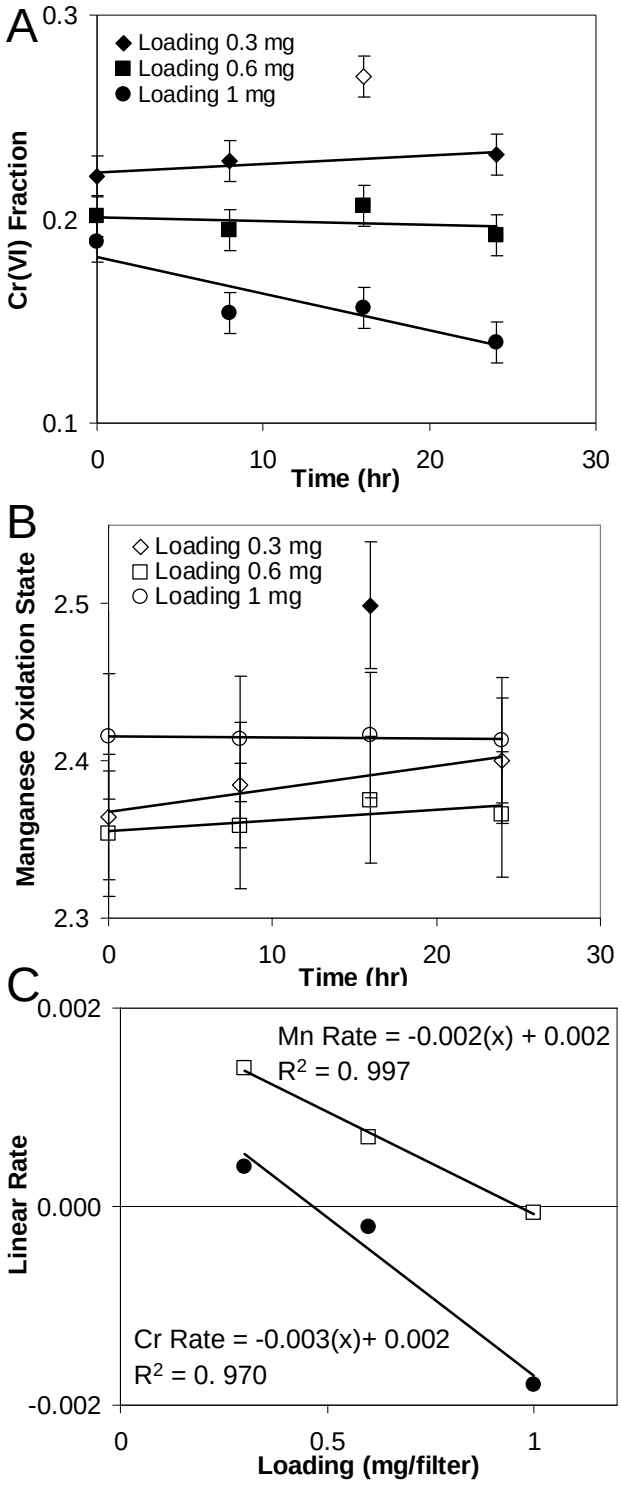
A
Loading 0.3 mg
Loading 0.6 mg
Loading 1 mg
Cr(VI) Fraction
0.3
0.2
0.1
0
10
20
30
Time (hr)
B
Loading 0.3 mg
Loading 0.6 mg
Loading 1 mg
Manganese Oxidation State
2.5
2.4
2.3
0
10
20
30
Time (hr)
C
Mn Rate = -0.002(x) + 0.002
R2 = 0. 997
Cr Rate = -0.003(x)+ 0.002
R2 = 0. 970
Linear Rate
0.002
0.000
-0.002
0
0.5
1
Loading (mg/filter)

Figure 3

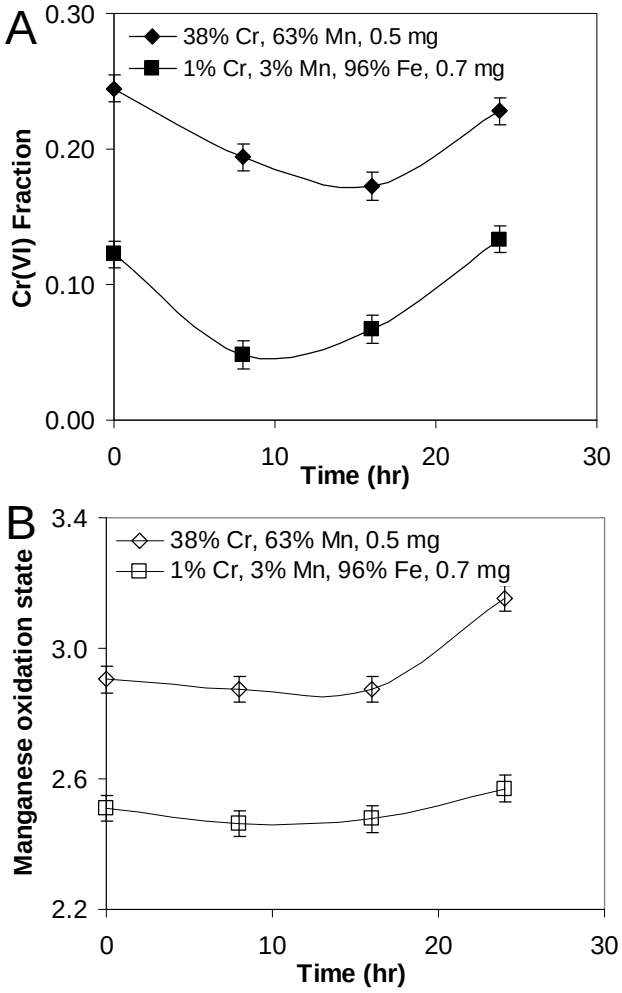
A
0.30
0.20
0.10
0.00
Cr(VI) Fraction
38% Cr, 63% Mn, 0.5 mg
1% Cr, 3% Mn, 96% Fe, 0.7 mg
0
10
20
30
Time (hr)
B
3.4
3.0
2.6
2.2
Manganese oxidation state
38% Cr, 63% Mn, 0.5 mg
1% Cr, 3% Mn, 96% Fe, 0.7 mg
0
10
20
30
Time (hr)

Figure 4

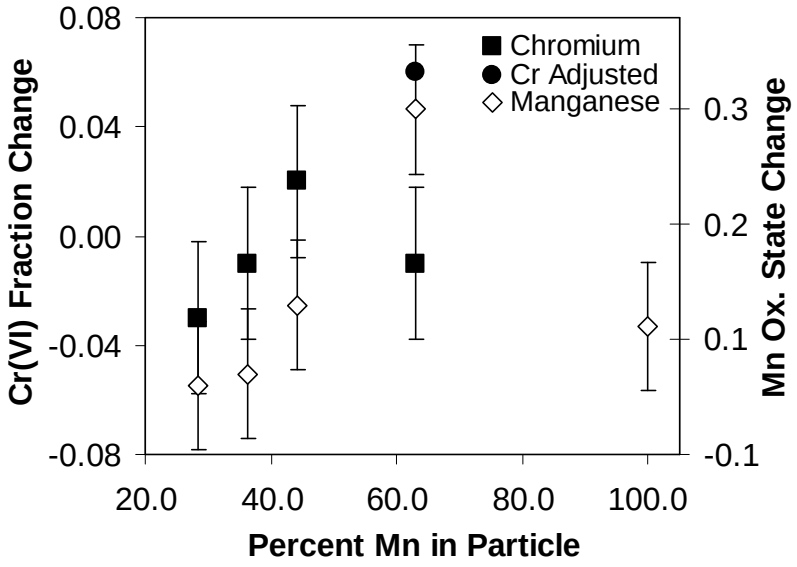
0.08
0.04
0.00
-0.04
-0.08
Cr(VI) Fraction Change
Chromium
Cr Adjusted
Manganese
0.3
0.2
0.1
-0.1
Mn Ox. State Change
20.0
40.0
60.0
80.0
100.0
Percent Mn in Particle

Figure 5

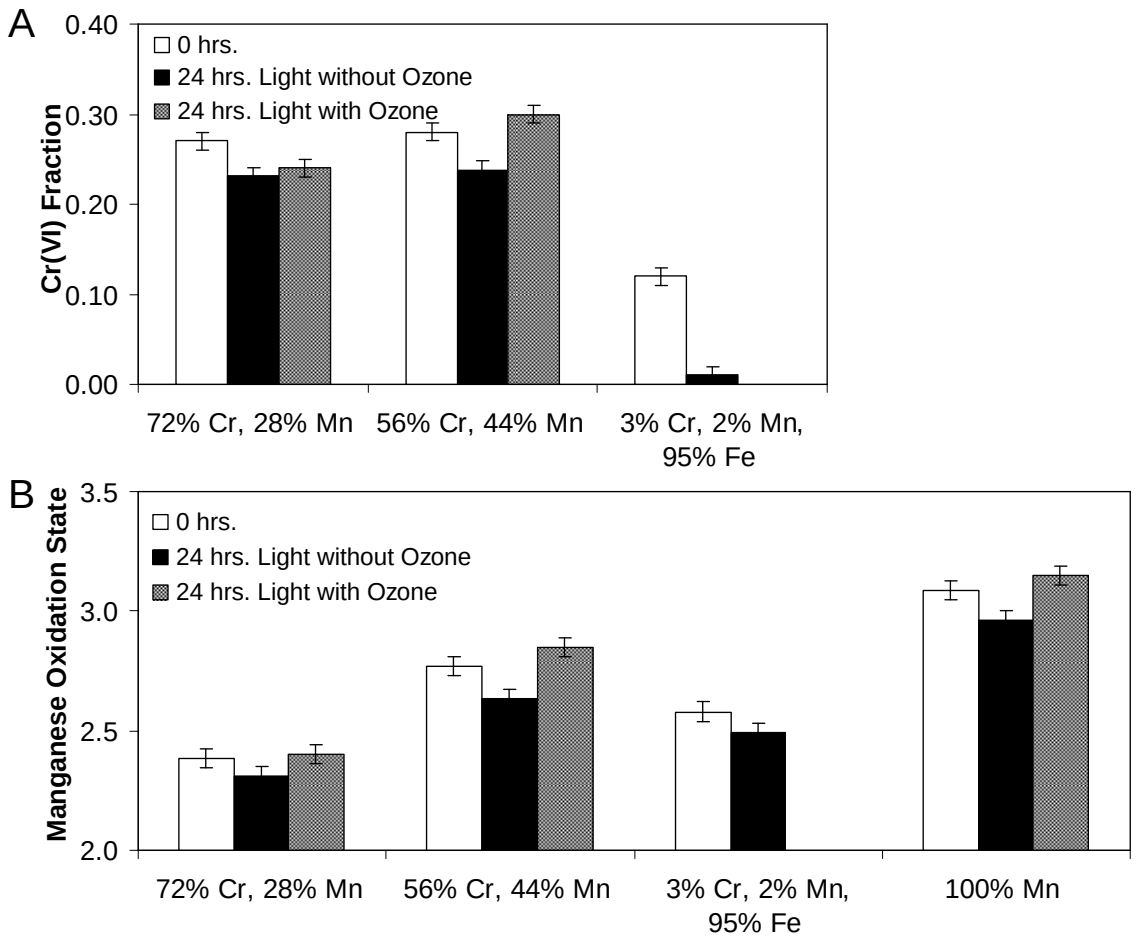
A
0.40
0.30
0.20
0.10
0.00
Cr(VI) Fraction
0 hrs.
24 hrs. Light without Ozone
24 hrs. Light with Ozone
72% Cr, 28% Mn
56% Cr, 44% Mn
3% Cr, 2% Mn, 95% Fe
B
3.5
3.0
2.5
2.0
Manganese Oxidation State
0 hrs.
24 hrs. Light without Ozone
24 hrs. Light with Ozone
72% Cr, 28% Mn
56% Cr, 44% Mn
3% Cr, 2% Mn, 95% Fe
100% Mn

Figure 6

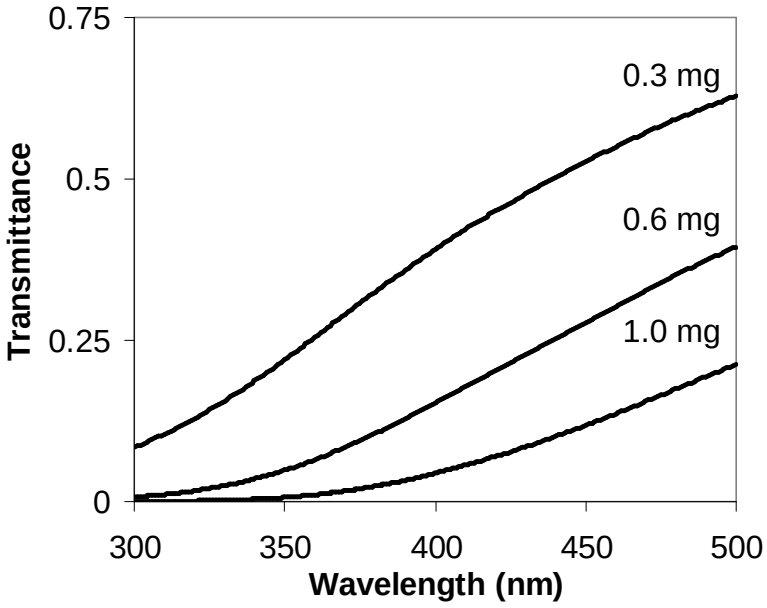
0.75
0.5
0.25
0
Transmittance
0.3 mg
0.6 mg
1.0 mg
300
350
400
450
500
Wavelength (nm)

Figure 7

1 **Table 1**

Standard	100% Mn		63% Mn-38% Cr				44% Mn-56% Cr		
	0 hrs	**24 hrs**	**0 hrs**	**8 hrs**	**16 hrs**	**24 hrs**	**0 hrs**	**24 hrs**	**24 hrs[1]**
Mn(II) phases	6%	6%	7%	8%	8%	7%	11%	10%	12%
Hausmannite (Mn_3O_4)	47%	41%	58%	58%	58%	35%	59%	55%	65%
Ramsdellite (MnO_2)	47%	53%	35%	34%	34%	58%	30%	35%	23%

2 [1]without O_3